nature energy

Article

https://doi.org/10.1038/s41560-023-01356-y

Inorganic glass electrolytes with polymer-like viscoelasticity

Received: 9 April 2023

Accepted: 16 August 2023

Tao Dai[1], Siyuan Wu[1], Yaxiang Lu[1,2,3,4] ✉, Yang Yang[1], Yuan Liu[1], Chao Chang[1], Xiaohui Rong[1,3], Ruijuan Xiao[1], Junmei Zhao[5] ✉, Yanhui Liu[1], Weihua Wang[1], Liquan Chen[1] & Yong-Sheng Hu[1,2,3,4] ✉

Solid-state batteries offer an alternative promising power source for electric vehicles. However, the interfacial mechanical stability of inorganic electrolytes is inferior to that of organic electrolytes. A high stack pressure (several to hundreds of megapascals) is often required to maintain intimate contact with electrodes. Here we report a class of viscoelastic inorganic glass (VIGLAS) to serve as solid electrolytes by simply replacing chlorine of tetrachloroaluminates with oxygen. The VIGLAS possesses high ionic conductivity (~1 mS cm^{-1} at 30 °C) for both Li$^+$ and Na$^+$, superior chemo-mechanical compatibility with 4.3 V cathodes and the ability to enable pressure-less Li- and Na-based solid-state batteries (<0.1 MPa). The low melting temperature (<160 °C) allows the electrolytes to efficiently infiltrate electrode materials, akin to a liquid battery. Additionally, the deformability of the electrolytes facilitates the feasibility of scale-up through the production of thin films via a rolling process.

Solid-state batteries (SSBs) have attracted intensive research interest, mainly owing to the expected higher energy density and higher safety than conventional liquid batteries[1]. However, it has been challenging to maintain a chemo-mechanically stable interface between solid electrolytes and electrode materials in the development of SSBs[2]. Regarding the anodes of SSBs, both lithium metal and sodium metal anodes are extensively studied owing to their high energy density. Plenty of work has been reported to effectively suppress the chemo-mechanical degradation of the interface on the anode side, such as dendrite growth and side reactions[3–6]. On the cathode side of SSBs, however, there has still been a trade-off between the chemical stability (oxidative resistance) and mechanical compatibility (intimate interfacial contact) with high-voltage cathode materials[7].

For instance, organic polymer electrolytes, such as polyethylene oxide (PEO), have shown mechanical compatibility with electrodes without high additional stack pressure, but they are chemically unstable with high-voltage cathodes[8]. Among current inorganic solid electrolytes, garnets exhibit high chemical stability but cannot accommodate the volume change of electrodes owing to the high modulus and brittleness[9]. The promising sulfide-based and chloride-based SSBs both require high external stack pressure (several to hundreds of megapascals) to maintain intimate contact with electrode materials during operation[10,11]. However, the additional components used to apply pressure would decrease the energy density, and battery packs impose serious upper limits on cell stack pressure, which is one of the most critical constraints for the successful design of SSB cells (the ideal pressure being below 0.1 MPa)[1]. Therefore, it would be of great importance if inorganic solid electrolytes could also be equipped with polymer-like mechanical properties so as to enable pressure-less inorganic SSBs.

In this Article, we report a class of viscoelastic inorganic glass (VIGLAS) serving as solid electrolytes with high ionic conductivities (~1 mS cm^{-1}) for both Li$^+$ and Na$^+$, which can simultaneously achieve both chemical stability and mechanical compatibility with high-voltage

---

[1]Key Laboratory for Renewable Energy, Beijing Key Laboratory for New Energy Materials and Devices, Beijing National Laboratory for Condensed Matter Physics, Institute of Physics, Chinese Academy of Sciences, Beijing, China. [2]College of Materials Science and Optoelectronic Technology, University of Chinese Academy of Sciences, Beijing, China. [3]Huairou Division, Institute of Physics, Chinese Academy of Sciences, Beijing, China. [4]Yangtze River Delta Physics Research Center Co. Ltd., Liyang, China. [5]Institute of Process Engineering, Chinese Academy of Sciences, Beijing, China.
✉e-mail: yxlu@iphy.ac.cn; jmzhao@ipe.ac.cn; yshu@iphy.ac.cn

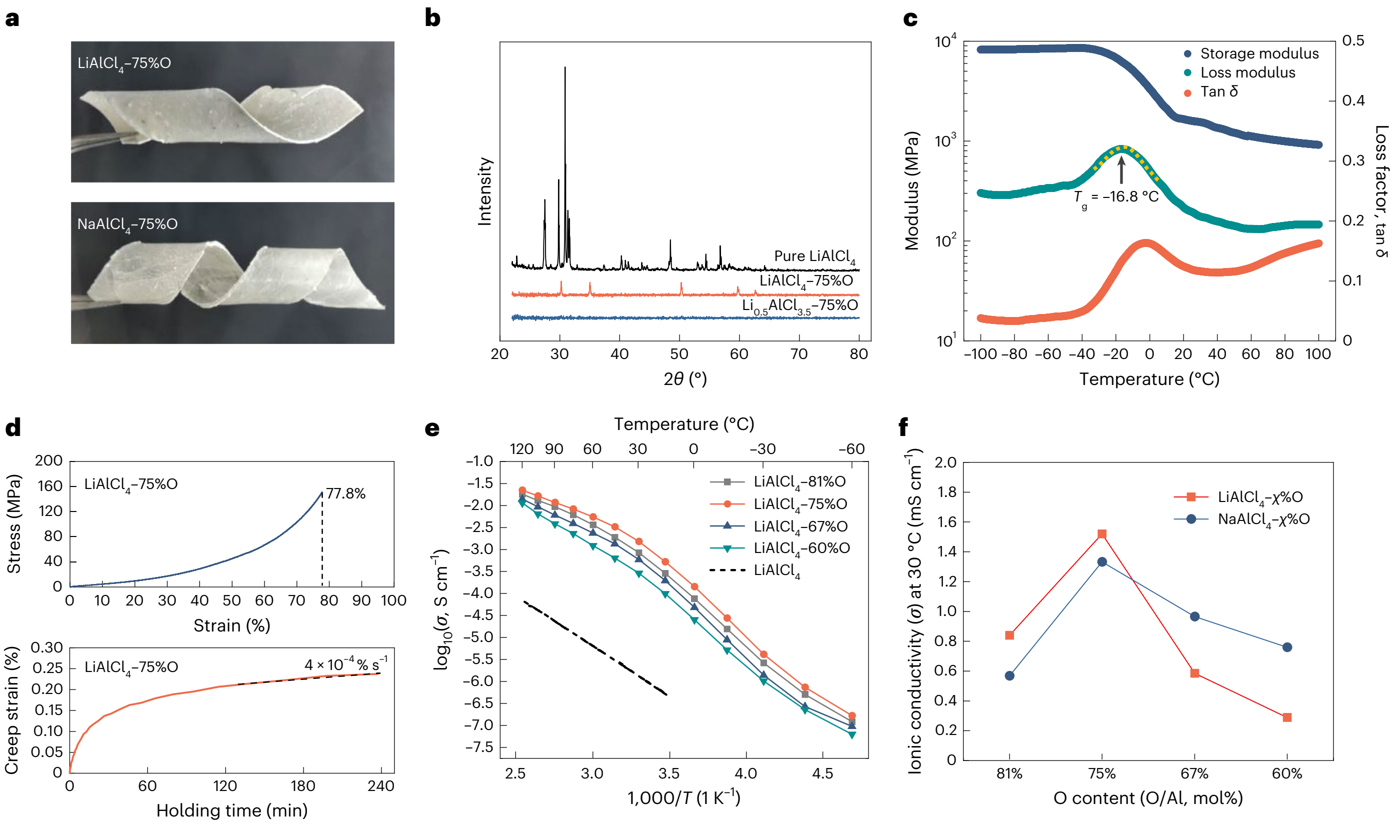

Fig. 1 | Polymer-like characteristics of MACO. a, Winding membranes of $LiAlCl_4$–75%O ($LiAlCl_{2.5}O_{0.75}$, O/Al ratio of 75%, LACO75) and $NaAlCl_4$–75%O ($NaAlCl_{2.5}O_{0.75}$, O/Al ratio of 75%, NACO75) obtained by the rolling process. **b**, X-ray diffraction spectra of $LiAlCl_4$, LACO75 and $Li_{0.5}AlCl_2O_{0.75}$. **c**, Dynamic moduli and loss tangent of LACO75 in DMA tests at various temperatures. The loss tangent δ is the ratio of storage modulus to loss modulus. **d**, Stress–strain curve of LACO75 under quasi-static loading by compression with a strain rate of $10^{-4}\ s^{-1}$ at 30 °C and creeping curve of LACO75 under an applied load of 0.1 MPa at 60 °C. The end of the stress–strain curve is due to reaching the maximum range of the compression device and does not represent fracture failure. **e**, The temperature-dependent conductivity (σ) of LACO with different oxygen contents. The ionic conductivity data of $LiAlCl_4$ are obtained from ref. 15. **f**, The ionic conductivity of LACO and NACO with different oxygen contents at 30 °C. χ represents different oxygen contents, from 60% to 81%.

cathode materials, enabling pressure-less (<0.1 MPa) inorganic Li- and Na-based SSBs. These VIGLAS electrolytes of $MAlCl_{4-2x}O_x$ (MACO, M = Li, Na, $0.5 < x < 1$) are synthesized by adding a high content of oxygen into tetrachloroaluminates to replace chlorine (Supplementary Note 1). Along with the increase of the oxygen content, the oxygen-containing tetrachloroaluminates would transform from brittle molten salts to ductile glasses (brittle to ductile transition) at room temperature (RT). The polymer-like viscoelasticity endows them with the ability to endure deformation under pressure-less operating conditions. Meanwhile, these VIGLAS electrolytes also have adequate chemical stability to resist the high-voltage decomposition (4.3 V for both $LiAlCl_{4-2x}O_x$ (LACO) and $NaAlCl_{4-2x}O_x$ (NACO)). Moreover, the melting temperature of MACO is below 160 °C, allowing complete infiltration into electrode materials resembling liquid electrolytes to obtain excellent ionic percolation and scalability.

Discovery of MACO with viscoelasticity

Tetrachloroaluminates ($MAlCl_4$, M = Li, Na) are typical molten salts with quite low melting points (146 °C and 157 °C for $LiAlCl_4$ and $NaAlCl_4$, respectively)[12–14] and rigid ionic bonds. They appear as liquids with low viscosities when melted at high temperature, and once cooled down, the liquids solidify to crystals with high hardness and fragility (Supplementary Video 1). Conversely, as oxygen is added to $MAlCl_4$ melts to replace chlorine, their viscosity increases dramatically at high temperature (Supplementary Video 2) and the solidified products possess a reduced hardness and enhanced deformability at RT. For example, when the oxygen content reaches 75% (O/Al ratio of 75%), $LiAlCl_4$–75%O ($LiAlCl_{2.5}O_{0.75}$, LACO75) and $NaAlCl_4$–75%O ($NaAlCl_{2.5}O_{0.75}$, NACO75) turn out to be easily rolled into thin films and cut into certain shapes like PEO polymers (Supplementary Video 3 and Fig. 1a). Additionally, the LACO75 film can endure repetitive bending (Supplementary Video 4), demonstrating polymer-like deformability. It should be noted that the hardness of LACO will increase slightly after being stored for a period of time after synthesis, but it still retains viscoelastic properties (Supplementary Note 2).

To understand this phenomenon, X-ray powder diffraction tests were firstly carried out to probe the structural changes due to the oxygen substitution. As shown in Supplementary Fig. 1a,b, the $MAlCl_4$ patterns gradually fade away with increasing oxygen contents while very faint signals of LiCl and NaCl are present for MACO, indicating that the main phase of MACO is amorphous. However, the corresponding mechanical and electrochemical performance of the main phase is not affected by the presence of small amounts of LiCl and NaCl. For example, the LiCl in LACO75 was further eliminated when the Li/Al ratio was reduced to 0.5 and the $Li_{0.5}AlCl_2O_{0.75}$ becomes a completely amorphous phase (Fig. 1b). A detailed comparison of LACO75 and $Li_{0.5}AlCl_2O_{0.75}$ is shown in Supplementary Fig. 2 and Note 3.

To determine the origin of MACO's viscoelasticity, dynamic mechanical analysis (DMA) tests were performed on LACO75 and NACO75 at various temperatures. In Fig. 1c and Supplementary Fig. 3d, as the temperature rises, the storage moduli (elastic moduli, E_{Li} = 1.5 GPa and E_{Na} = 3.2 GPa at 30 °C) begin to decrease and the loss moduli (measuring the energy dissipation) start to rise and peak at −16.8 °C and −25.5 °C, respectively, indicating that the glass transition processes ($T_{g,Li}$ = −16.8 °C and $T_{g,Na}$ = −25.5 °C, signified by the peak of the loss modulus) occur below RT. The oxygen content has no noticeable effect on the T_g values of LACO, which are all lower than RT (Supplementary Fig. 4). It is noteworthy that viscoelasticity is not exclusive to polymers: any glasses in a glassy state can achieve viscoelasticity by transforming from 'frozen liquids' into 'supercooled liquids' with superplasticity (viscous flow under stress, without crystal-like defects of dislocation climb and glide), as long as the temperature rises above T_g. Therefore, it is the T_g below RT that endows MACO75 glasses with viscoelasticity. Since the T_g of LACO75 is below RT, LACO75 exhibits strong deformability (>77.8% strain) under quasi-static loading by compression and shows a viscoelastic creep rate of 4×10^{-4}% s^{-1} (Fig. 1d). The viscoelastic creep behaviour is so important because it endows MACO with the ability to repeatedly deform without defects and structure failure, given the cyclic stress imposed by the volume change of electrode material particles.

Then, differential scanning calorimetry (DSC) was also adopted to conduct thermal analysis on MACO in the high temperature range (Supplementary Fig. 3a,b). Distinct endothermic peaks of $MAlCl_4$ at around 150 °C corresponding to the melting processes are clearly observed. With increasing oxygen contents, the endothermic peaks of MACO shift to lower temperatures (128 °C for LACO and 154 °C for NACO) and finally disappear (for LACO, see Supplementary Fig. 3c). Note that the endothermic peaks do not represent the melting processes of the main phase of MACO glasses but rather the melting processes of unreacted M_xAlCl_{3+x} phase, which serves as a 'plasticizer' in MACO glasses. This can be verified by the weak signals of M_xAlCl_{3+x} phases in the XRD patterns for low oxygen contents (Supplementary Fig. 1a,b). When the oxygen contents are further increased (≥67% for LACO and ≥75% for NACO), exothermic peaks appear in the high temperature region, signifying that the crystallization processes appear in the high temperature region (T_c), demonstrating that the crystallization process of MACO had been hindered during cooling after synthesis. Notably, the endothermic peaks disappeared at high oxygen content (86% and 81% O for LACO and NACO, respectively), indicating that there are no liquid phases during the heating processes and that these oxygen contents are close to the maximum solubilities of oxygen.

It is worth noting that the ionic conductivities of $LiAlCl_4$ and $NaAlCl_4$ have been reported by Weppner et al. as 1.2×10^{-6} S cm^{-1} and 3.5×10^{-7} S cm^{-1}, respectively[15]. However, we found that, after adding oxygen into $MAlCl_4$ to replace chlorine, the ionic conductivities of these classical solid electrolytes are boosted by three orders of magnitude, first increasing and then reaching the highest ionic conductivities at 75% oxygen content (1.52×10^{-3} S cm^{-1} for LACO75 and 1.33×10^{-3} S cm^{-1} for NACO75 at 30 °C) (Fig. 1e,f and Supplementary Fig. 5a). The activation energies of LACO75 and NACO75 can be found in Supplementary Fig. 5b. The S-shaped curves of LACO indicate the rapid increase of the ionic conductivity between −30 °C and 30 °C, verifying the glass transition process.

Mechanisms of glass formation and ionic conduction

To determine the glass formation and ionic conduction mechanisms of as-prepared MACO75, LACO75 is taken as an example to be simulated by ab initio molecular dynamics (AIMD) and the simulation results are further validated by neutron pair distribution function (PDF) analysis in Supplementary Fig. 6. Due to the non-directional and unsaturated nature of the ionic bonding between Li^+ and $AlCl_4^-$, ions of the $LiAlCl_4$ melts are easily rearranged into crystals (Supplementary Fig. 7a) during condensation. The extended structure of $LiAlCl_4$ is composed of distorted $LiCl_6$ octahedra and $AlCl_4$ tetrahedra, where two $LiCl_6$ octahedra link via a common edge to form Li_2Cl_{10} dimers, existing in the 'pseudo-layers' between the isolated $AlCl_4$ tetrahedra (Supplementary Fig. 7b)[16]. However, the structure of LACO75 obtained by AIMD is completely disordered, the oxygen in LACO75 acts as a bridge to link the isolated Al atoms together, forming Al–O–Al segments or networks (Supplementary Fig. 7c,d). The strong Al–O bonds are difficult to break in molten LACO75, and the rearrangement of atoms is restricted by Al–O–Al networks during condensation, thus forming LACO75 glass. The origin of the above features lies in the fact that oxygen is divalent while chloride is monovalent. Hence, the bridging oxygen (BO) serves as the weaver of Al–O–Al networks, but the chloride prefers to coordinate with single Al atom as a network breaker (just like Na_2O in Na_2O–SiO_2 glass). In this sense, the appropriate ratio of O to Cl can ensure a proper size of the Al–O–Al network and the remaining $[AlCl_x]^{3-x}$ anion groups that are not connected by oxygen also act as a plasticizer, which both help to lower the T_g of LACO. Supplementary Note 4 also delves into the effects of the lithium and oxygen contents on the structure of LACO. To further investigate the bonding between aluminium and oxygen, Fourier transform-infrared (FTIR) spectroscopy and Raman spectroscopy were utilized (Supplementary Fig. 8). In the FTIR spectra, a peak at approximately 492 cm^{-1} corresponding to $AlCl_4^-$ noticeably diminishes with the addition of oxygen, while a new peak at around 693 cm^{-1} corresponding to the Al–O bond gradually emerges[17]. In the case of Raman spectra, obtaining a clear signal becomes challenging when oxygen is introduced owing to strong fluorescence effects. However, a new peak associated with the Al–O bond (~262 cm^{-1}) is still observed in the Raman spectra of LACO75[18]. Simultaneously, the peak of $AlCl_4^-$ is notably weakened compared with the Raman spectra of $LiAlCl_4$. Both the FTIR and Raman spectra demonstrate a structural transformation from $AlCl_4^-$ to $AlO_xCl_y^{3-2x-y}$, further validating the structure obtained by AIMD.

To understand the Li^+ transport mechanism in LACO75, the atom position distribution of all elements in $LiAlCl_4$ and LACO75 are presented in Fig. 2a,b and Supplementary Fig. 11. The movements of Li and Cl are substantially enhanced while the Al and O slightly move in LACO75, which is verified by the mean square displacement (MSD) of each type of ions in Fig. 2c. Although the movement of Cl is greatly promoted, it is just rotating around the Al centre with no migration events observed (not Al^{3+}, Cl^- or O^{2-} conductors, as shown in Supplementary Fig. 12). The two closest distances for Li^+ hopping in $LiAlCl_4$ are within the Li_2Cl_{10} dimers: 4.22 Å and 4.88 Å (Fig. 2d). However, the segment of LACO75 shown in Fig. 2e demonstrates that the Li–Li distance (2.55 Å and 3.08 Å) is pulled much closer by O, which is also confirmed in the radial distribution function (RDF) of Li–Li in $LiAlCl_4$ and LACO75 (Fig. 2f). In addition, the Al–Al distance and corresponding RDF of $LiAlCl_4$ and LACO75 are also compared in Supplementary Fig. 13. It is shown that BOs considerably narrow the distance of Al–Al (2.55 Å versus 4.63 Å, less than twice the distance of Al–O bonds), proving the existence of Al–O–Al chains or networks.

Based on the favourable structural factors involving the closer Li^+ hopping distance and the existence of Al–O–Al chains, two different transport mechanisms for Li^+ were observed. As shown in Fig. 2g,h, three lithium ions all rotate around the same oxygen and one of them hops and coordinates with another adjacent O on the same Al–O–Al segment, representing the direct Li^+ hopping process thanks to the closer hopping distance. Meanwhile, as presented in Fig. 2i,j, the Al–O–Al chain swings by itself and drives the surrounding Li^+ and Cl^- ions to migrate together. According to the free volume model[19], the free volume in the glass increases drastically above T_g, so that segment motion is activated. Owing to the completely disordered structure, the positive and negative charge centres of localized Al–O–Al segments may not overlap (dipole moment), so the movement or rotation of the segments would be triggered under the electric field. Upon that, the Li^+ transference number of LACO75 was measured to be 0.69 at 30 °C (Supplementary Fig. 14a,b). The Na^+ transference number was measured to be 0.91 and the electronic conductivity of LACO75 and NACO75 are 4.7×10^{-8} S cm^{-1} and 4.3×10^{-8} S cm^{-1}, respectively, at 30 °C, as illustrated in Supplementary Fig. 14c–f. Even though a non-unity ion

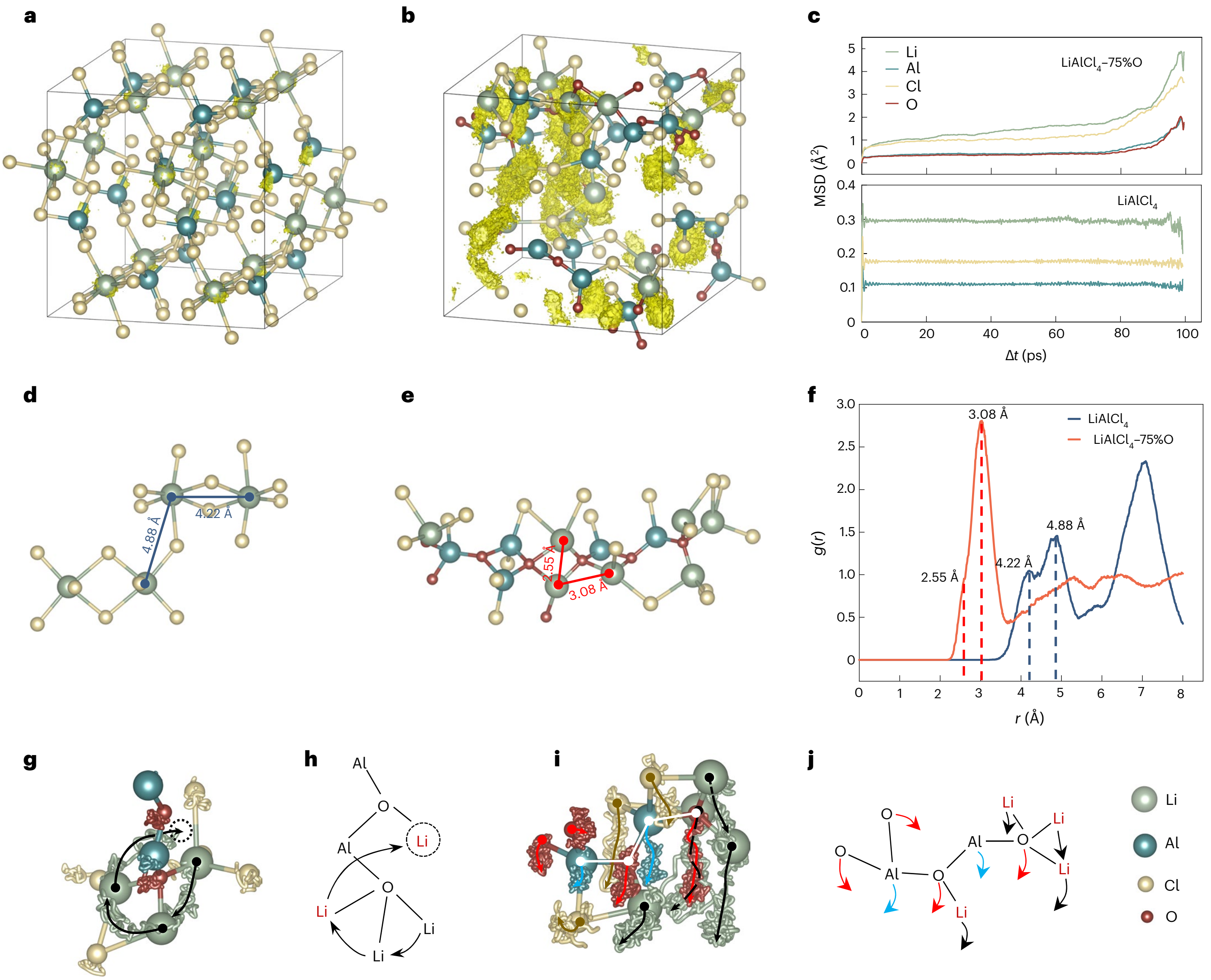

Fig. 2 | Li$^+$ transport mechanism in LACO75 simulated by AIMD at 300 K. **a**,**b**, The atom position distribution of Li in LiAlCl$_4$ (**a**) and LACO75 (**b**). The box size used for the simulation of LiAlCl$_4$ and LACO75 is 1.4 × 1.4 × 1.3 nm^3. Green, blue, yellow and red spheres represent Li, Al, Cl and O, respectively. The LACO75 structure is generated by substituting 37.5% of Cl with O in the LiAlCl$_4$ structure, running AIMD at 600 K for 30 ps and then cooling down to 300 K. The bright-yellow points signify the movement trajectories of Li$^+$ in LiAlCl$_4$ and LACO75 during 100 ps. **c**, The MSD of Li, Al, Cl and O in LiAlCl$_4$ and LACO75 during 100 ps. The Δt refers to the time interval during the AIMD simulation. **d**, **e**, Microstructural fragments with the shortest Li$^+$ transition distances of LiAlCl$_4$ (**d**) and LACO75 (**e**). **f**, The RDF of Li–Li in LiAlCl$_4$ and LACO75. The r represents the distance between different Li ions. **g**, **h**, Movement trajectories of Li, Al, Cl and O elements in a hopping event (**g**) and the corresponding schematic diagram of Li$^+$ migration (**h**). The schematic diagram shows that three Li$^+$ revolve around oxygen and one of them (red) hops to and coordinates with another adjacent oxygen on the same Al–O–Al chain segment. **i**, **j**, Movement trajectories of Li, Al, Cl and O elements on a swinging Al–O–Al segment (**i**) and the corresponding schematic diagram denoting the movement directions of all the elements (**j**). The movement trajectories are obtained by recording the true position of each atom every 0.01 ps during the ion hopping events and then overlaying the movement-by-movement positions of these moving atoms on the initial structure. The arrows in **h** and **j** signify the moving directions of elements.

transference number would decrease the rate performance of SSBs, the single Li$^+$ conductivity of LACO75 under steady-state polarization still remains relatively high at 1.05 mS cm^{-1} at 30 °C. Besides, as shown in Supplementary Fig. 15 and Note 5, the activation energy in the high temperature range (30–105 °C) calculated by molecular dynamics simulations was found to be 0.30 eV, which closely matches the experimental results (0.33 eV). This close agreement further confirms the plausibility of the ionic conduction mechanism observed in the AIMD simulations. We believe that this segment-motion-promoting Li$^+$ transport mechanism in inorganic LACO75 probably exists in other inorganic glasses above T_g, which would help inorganic glasses to obtain an additional promoter of ionic conduction, apart from the Li$^+$ hopping in the glassy state. For example, Li$^+$ may be brought by the segment motion to a more favourable position with closer hopping distance and then hop.

Chemo-mechanical stability with high-voltage cathodes

The compatibility of as-prepared MACO with electrodes was then measured to evaluate their feasibility as solid electrolytes. As shown in Supplementary Fig. 16a,b, the oxidation potentials of LACO75 and NACO75 are 3.85 V and 3.9 V, respectively. However, when cyclic voltammetry (CV) tests were performed in the range of 3–5.5 V (Supplementary Fig. 16c), it is clearly demonstrated that the oxidation currents of LACO75 and NACO75 both reduce rapidly after the first cycle, implying that a passivation layer is generated at the high oxidation potential

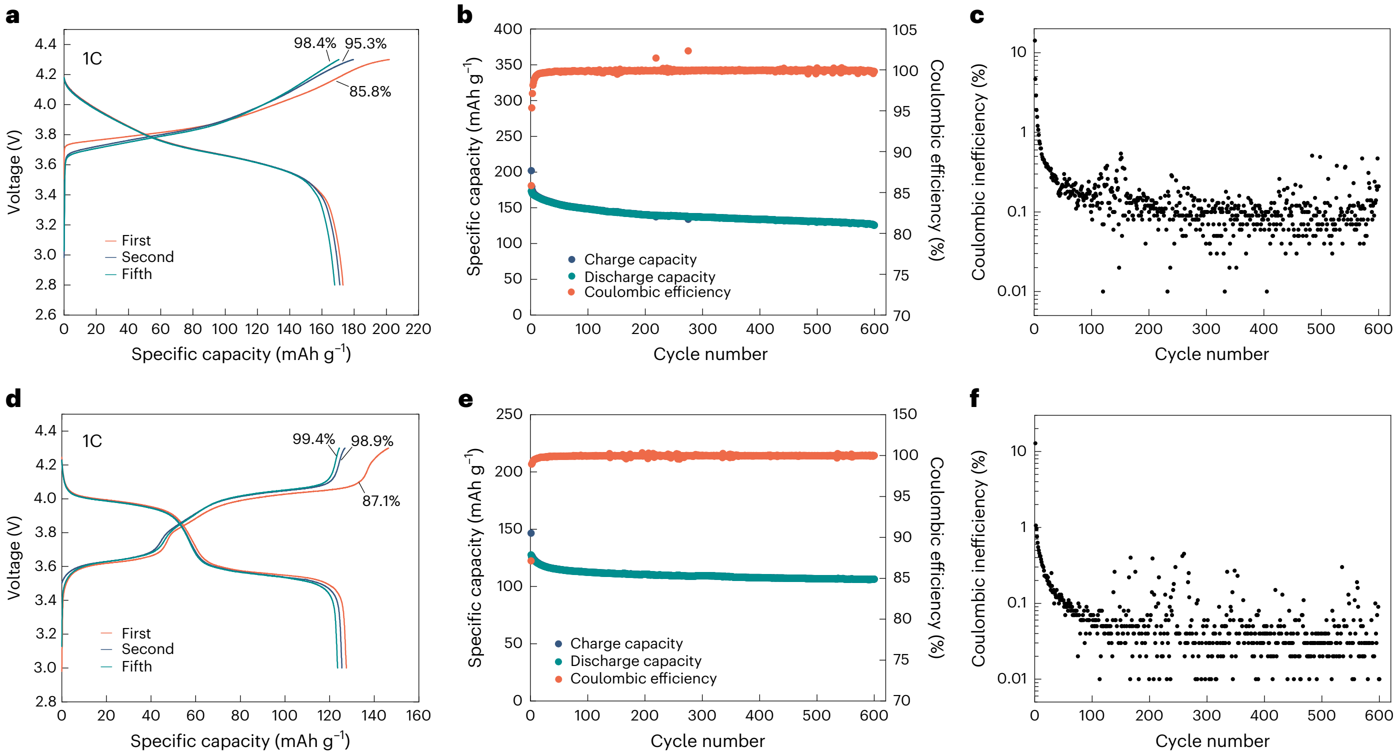

Fig. 3 | Electrochemical performance of MACO in SSBs. a–c, Charge and discharge profiles (**a**), cycling performance (**b**) and Coulombic inefficiency (**c**) of the Li/LLZTO/LACO75–NCM622 cell cycled at 1C and charged to 4.3 V at 60 °C. **d–f**, Voltage curves (**d**), capacity retention (**e**) and Coulombic inefficiency (**f**) of the Na/NASICON/NACO75–NVOPF cell cycled at 1C between 3.0 V and 4.3 V at 60 °C.

to prevent further decomposition. The composition of this passivation layer was probed by X-ray photoelectron spectroscopy (XPS) analysis and density functional theory (DFT) calculations. As seen in Supplementary Fig. 16d, comparing the XPS spectra of the pristine and charged LACO75–$LiNi_{0.6}Co_{0.2}Mn_{0.2}O_2$ (NCM622) composite cathodes, the O 1*s* peak intensity of LACO75 is weakened and a small amount of Al_2O_3 in the Al 2*p* spectra is generated after being charged to 4.3 V (ref. 20). According to the Cl 2*p* spectra (Supplementary Fig. 17b) and compared with the experimental $LiAlCl_4$ spectra, it is confirmed that $LiAlCl_4$ also exists. The DFT calculation results further suggest that LACO75 decomposes into Al_2O_3 and $LiAlCl_4$ when oxidized (Supplementary Fig. 17a). Both $LiAlCl_4$ and Al_2O_3 have been proven to be highly oxidation resistant[21,22], which is why LACO75 is compatible with high-voltage cathode materials. To further evaluate the oxidation resistance of MACO in SSBs, we chose the Li/Na-metal-stable electrolyte $Li_{6.4}La_3Zr_{1.4}Ta_{0.6}O_{12}$ (LLZTO) and $Na_3Zr_2Si_2PO_{12}$ (NASICON) to minimize the influence from the anode side and fabricated Li/LLZTO/LACO75–NCM622 cells and Na/NASICON/NACO75–$Na_3(VOPO_4)_2F$ (NVOPF) cells without any coatings on the NCM622 and NVOPF particles (Supplementary Fig. 20a,b). In addition, all the cell measurements were conducted without additional pressure applied. As shown in Fig. 3, the cells were charged to 4.3 V at 1C and cycled for 600 times at 60 °C. The Li cell delivers an initial discharge capacity of 173 mAh g^{-1} and retains 125 mAh g^{-1} after cycling, while the Na cell shows an initial discharge capacity of 127 mAh g^{-1} and capacity retention of 83.5%. The Coulombic efficiencies rise rapidly to 99.9% in the initial cycles, demonstrating compatibility with 4.3 V cathodes. Then, the cells were cycled at 0.1C for 100 times at 30 °C with capacity retention of 96.0% and 93.1%, respectively (Supplementary Fig. 18). Furthermore, cells with commercially thick cathodes were also tested. The Li/LLZTO/LACO75–NCM622 cell and Na/NASICON/NACO75–NVOPF cell with active mass loadings of 22.2 mg cm^{-2} and 23.9 mg cm^{-2} were cycled to 4.3 V for 100 cycles at 0.1C and 60 °C (Supplementary Fig. 19a,b,d,e). After the initial three cycles for stabilization, the cells exhibited specific capacities of 178 mAh g^{-1} and 124.7 mAh g^{-1} and eventually have capacity retention of 86.1% and 90.6%, respectively, after cycling.

Features for scalability

On the basis of the analysis above, it has been demonstrated that MACO are very promising electrolytes to enable pressure-less Li- or Na-based SSBs. Regarding processability for practical applications, the low melting temperatures of 128 °C and 154 °C can facilitate the liquid MACO to completely infiltrate the tortuous porous structures of electrodes and provide intimate ionic contacts and favourable ionic percolation for thick cathodes (mass loading >20 mg cm^{-2}) (Fig. 4a)[23]. Cross-sections of thick NCM622 and NVOPF cathodes fabricated by the melt infiltration process are shown in Supplementary Fig. 19c,f, in which the cathode particles are closely embedded in the cathode matrix.

In addition, melt infiltration is also of utmost importance for the adhesion force between electrolyte and cathode particles, considering the fact that the actual microscopic contact area between electrode materials and solid electrolytes is too small for most of the current inorganic solid electrolytes[24]. The limited actual microscopic contact area not only restricts the ion transport path but also greatly reduces the adhesion force between solid electrolytes and electrode materials, because the adhesion force is directly related to the microscopic contact area. When the adhesive force is not strong enough, the battery can only rely on additional pressure to maintain intimate contact between the solid electrolytes and electrode particles (sulfide SSBs).

In this sense, very similarly to PEO electrolytes, MACO's 'superplasticity' (T_g < RT) and large actual microscopic contact area due to melt infiltration both contribute to the pressure-less feature of MACO batteries. The homemade cell case is shown in Supplementary Fig. 21b, where a spring is only used to maintain the electrical contact (<0.1 MPa).

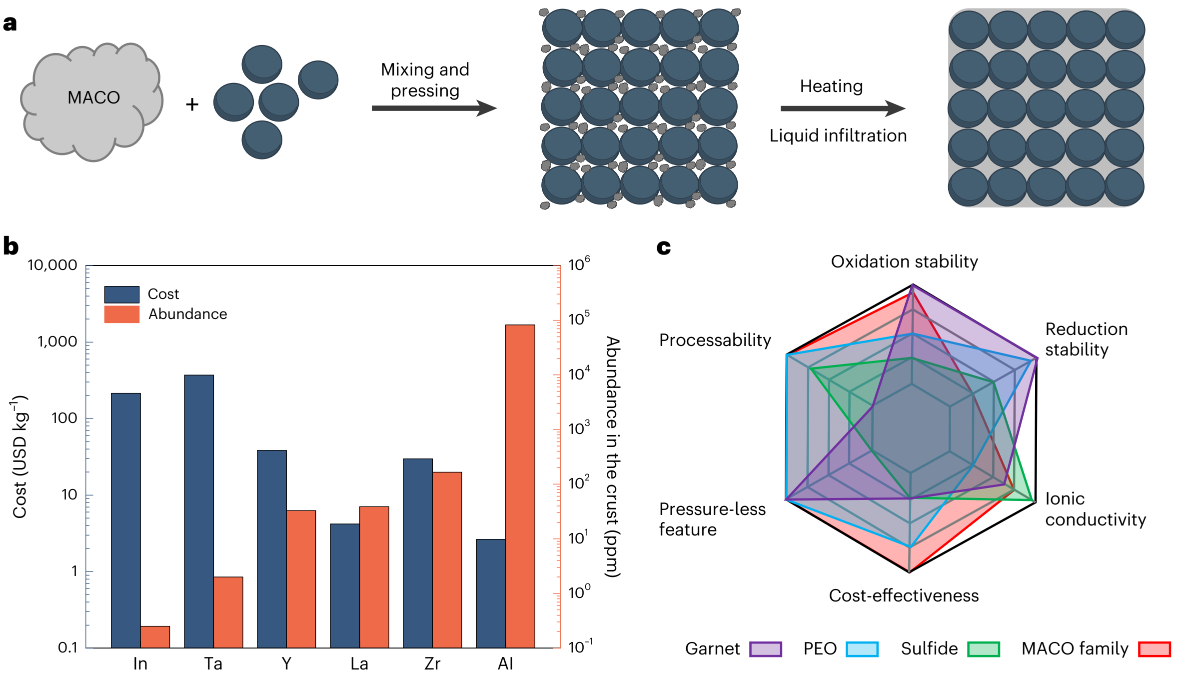

Fig. 4 | Processability and cost-effectiveness of MACO. a, A schematic diagram of the electrode fabrication process to achieve melt infiltration. **b**, The abundance and price of central metal elements in garnet, chloride and MACO electrolytes. **c**, Spider plot comparing the performance of garnet, PEO, sulfide and MACO-based electrolytes.

Moreover, MACO membranes can also be produced by a rolling process owing to the outstanding deformability (Supplementary Video 3).

Another important aspect that must be considered is the cost-effectiveness, which is one of the major obstacles to the commercialization of current inorganic solid electrolytes (garnets, sulfides and chlorides) owing to the complex manufacturing processes, low abundance of elements or high materials cost. However, MACO electrolytes possess advantages regarding all these issues. Firstly, the synthesis of MACO electrolytes is quite simple, only involving mixing and heating processes (Supplementary Note 6). Besides, Fig. 4b presents the abundance and price of central metal elements in garnet and chloride electrolytes. As the third most abundant element in the crust, Al also has the lowest price among all elements. Last but not least, the materials cost of MACO75 (US \$6.85 kg^{-1} for LACO75 and US \$1.95 kg^{-1} for NACO75; Supplementary Tables 1 and 2) is much lower than that of Li_6PS_5Cl (US \$319 kg^{-1})[25]. As an electrolyte derived from tetrachloroaluminate, the reaction product of MACO with moisture (HCl) is less toxic compared with H_2S, which would also help to lower production costs. In summary, the spider plot comparing the performance of garnet, PEO, sulfide and MACO-based electrolytes (Fig. 4c) shows that MACO-based electrolytes exhibit all-round advantages for application on the cathode side of SSBs.

Conclusions

We demonstrated that VIGLAS can serve as a promising solid electrolyte to enable pressure-less Li- and Na-based SSBs. These electrolytes are achieved by breaking the crystal structure of $MAlCl_4$ with the assistance of bridging oxygen to generate MACO with Al–O–Al networks. Owing to the movement/rotation of segments and the close ion hopping distance, the ionic conductivity is greatly boosted to above 1 mS cm^{-1}. The as-prepared LACO75 and NACO75 glasses have low T_g values of −16.8 °C and −25.5 °C, equipping them with viscoelasticity to behave like organic polymers and achieve excellent interfacial mechanical compatibility without additional stack pressure. MACO also demonstrates good chemical interfacial stability by maintaining stable cycling of SSBs with 4.3 V, high-voltage cathodes. Moreover, the outstanding mechanical property (deformability) and unique low-melting-temperature feature of MACO inherited from tetrachloroaluminates make them suitable for the rolling and melt infiltration assembly processes. We also found that, in addition to oxygen, sulfur can also promote the ionic conductivity of $LiAlCl_4$ (Supplementary Note 7). We strongly believe that there is a vast design space that the community could dedicate to vitrifying inorganic (non-)ionic conductors and screening for low-T_g VIGLAS to obtain polymer-like mechanical properties, which can contribute to fully tackling the issue of the mechanical instability of inorganic electrolytes and enable practical applications of pressure-less SSBs.

Methods

Preparation of electrolytes

Tetrachloroaluminates ($LiAlCl_4$ and $NaAlCl_4$) were prepared by mixing (grinding in a mortar) and heating anhydrous LiCl/NaCl (99.99%; Aladdin Co., Ltd) and anhydrous $AlCl_3$ (99.99%; Aladdin Co., Ltd) together in alumina or quartz crucibles at 200 °C. Initially, the freshly produced molten chloroaluminates were brown in colour owing to the presence of impurities. After adding small quantities of Al debris (10 mg, 99.99%; Aladdin Co., Ltd) to the molten $NaAlCl_4$ (10 g) for 5 h, the mixture became colourless. Oxygen was introduced into the chloroaluminates by adding Sb_2O_3. Under the protection of an inert atmosphere, stoichiometric amounts of Sb_2O_3 (99.99%; Aladdin Co., Ltd) and chloroaluminates were mixed and heated at 250 °C for more than 1 h to remove the volatilized gas (Supplementary Note 6). $Li_{2x}AlS_xCl_3$ electrolytes were synthesized by mixing and heating stoichiometric Li_2S (99.99%; Aladdin Co., Ltd) and $AlCl_3$ together at 200 °C.

Preparation of electrodes

NCM622 cathodes were fabricated according to the following process. First, NCM622 particles without any coating, LACO75, carbon nanotubes (CNTs) and polytetrafluoroethylene (PTFE) binder were mixed in a mass ratio of 70:20:5:5 (NCM622:LACO75:CNTs:PTFE). Then, the mixture was rolled to a film. Finally, the film was pressurized at 5 MPa to remove voids and heated to 200 °C for complete infiltration of cathode materials. NVOPF cathodes were prepared by using the same process, except that the NVOPF:NACO75:CNT:PTFE ratio was adjusted to 70:20:10:5. This is due to the relatively poor electronic conductivity of NVOPF, so the proportion of CNTs (the electronic conductive additive) was increased from 5% to 10%. The current densities and mass loadings of the NCM622 cathode and the NVOPF cathode for 1C cycling are 0.64 mA cm^{-2} (4 mg cm^{-2}) and 0.396 mA cm^{-2} (3.3 mg cm^{-2}), respectively. The current densities and mass loadings of the NCM622 cathode and the NVOPF cathode for 0.1C cycling at 30 °C are 0.053 mA cm^{-2} (3.3 mg cm^{-2}) and 0.058 mA cm^{-2} (4.8 mg cm^{-2}), respectively. The current densities of the NCM622 cathode and the NVOPF commercially thick cathodes for 0.1C cycling are 0.4 mA cm^{-2} and 0.3 mA cm^{-2}. The working electrodes used for LSV and CV tests were prepared from mixtures of MACO75, CNTs and PTFE with mass ratio of 90:10:5.

Assembly of SSBs

Schematic diagrams (not to scale) of the Li/LLZTO/LACO75–NCM622 and Na/NASICON/NACO75–NVOPF cells are shown in Supplementary Fig. 21a. The modification layer of the Li/LLZTO interface is produced by the energetic chemical reaction between $Zn(NO_3)_2$ and Li metal[26]. The Na/NASICON interface is modified by Na-Sn alloy (with a weight ratio of Na to Sn of 5:1)[27]. Firstly, the anodes were prepared and the interfaces of Li/LLZTO and Na/NASICON were modified. Then the cathodes were heated at 200 °C and the LLZTO/NASICON pellets (1 mm thick, bought from MTI. inc and Canrd. inc, respectively) were pressed onto the surface of the cathodes. After cooling down, all-solid-state cells were fabricated.

Computational details

The DFT calculations were performed employing the Vienna Ab Initio Simulation Package[28] by using the generalized gradient approximation and the Perdew–Burke–Ernzerhof (PBE) exchange–correlation function[29]. In order to obtain the LACO structures, the method used involves directly replacing two Cl in $LiAlCl_4$ with O, resulting in the hypothesized LACO structures. Subsequently, these hypothesized structures are run at a temperature of 600 K for 30 ps with a time step of 1 fs, causing them to fully melt. At this point, the predefined structures are lost, and the amorphous LACO structures are obtained when cooled down to 300 K. After obtaining the amorphous structures, AIMD was then performed with constant number–volume–temperature (*NVT*) at 300 K with 110 ps and 160 ps for $LiAlCl_4$ and $LiAlCl_{2.5}O_{0.75}$, respectively, to study ion transport properties and structural changes. To explain the changes of ionic conductivities at different temperatures, we performed molecular dynamics from 213 to 393 K in steps of 15 K using the many-body potential and interatomic forces trained by the Deep Potential MD method[30] for 3.5 ns with LAMMPS[31]. We also calculated results for $Li_{0.5}AlCl_2O_{0.75}$, $Li_{1.5}AlCl_3O_{0.75}$ and $LiAlCl_{3.5}O_{0.25}$ for comparison. The simulation steps for the above three compositions are shown as following. First, we used AIMD to melt the structures at 600 K to generate disordered structures. Then, we used DFT to relax the cell parameters to find the lattice constant with the lowest total energy. Next, we cooled the structures at a rate of 100 K ps^{-1} from 600 K to 300 K with a time step of 1 fs. Finally, we simulated their dynamical properties at 300 K for 50 ps with a time step of 1 fs. The MSD, atom distribution and the diffusion process were extracted as in our previous work[32]. All structure figures are presented by using VESTA software[33].

Characterization

DMA was implemented by using a TA Q800 dynamic mechanical analyser. All measurements were conducted in the three-point bending mode. The dynamic temperature ramp test was performed with a heating rate of 2 °C min^{-1} at 1 Hz. The creep curves were also obtained by using a TA Q800 in the three-point bending mode under an applied load of 0.1 MPa at 60 °C. The stress–strain curves of LACO75 were obtained by compression under quasi-static loading with a strain rate of 10^{-4} s^{-1} at 30 °C using an Instron 3400 mechanical tester. The X-ray diffraction patterns were collected by using a D8 Bruker X-ray diffractometer with Cu Kα radiation (λ = 1.5405 Å). A Hitachi S-4800 was used for scanning electron microscopy (SEM) analysis. The DSC tests were conducted on a differential scanning calorimeter (Mettler-Toledo, DSC1) in Ar atmosphere at a scanning rate of 10 °C min^{-1} from 0 °C to 250 °C. XPS spectra were probed by using an ESCALAB 250 Xi (ThermoFisher). The ionic conductivities of the MACO were measured by a.c. impedance with an amplitude of 50 mV in the frequency range from 1 MHz to 1 Hz (IM6e, Zahner). The sample was sandwiched between two tungsten foil blocking electrodes. All Nyquist plots for ionic conductivity measurements can be found in Supplementary Fig. 22. On the basis of the Nyquist plots of the full cell, Supplementary Fig. 25 and Supplementary Table 4 also present the electrochemical impedance spectroscopy analysis and fitting for the Li|LLZTO|LACO75–NCM622 cell. Galvanostatic charge–discharge performance tests were performed with a Land CT2001A battery test system. The neutron total scattering data were collected at the Multi-Physics Instrument in the Q range of 0.45–50 Å^{-1} at China Spallation Neutron Source (CSNS). Samples were sealed into thin-walled Zr-Ti cans with diameter of 9 mm in a helium-filled glove box before acquisition. The NPD patterns were refined using GSAS-II software[34]. Neutron PDF results were analysed using PDFgui software[35].

Data availability

The data that support the findings of this study are available within this article and its Supplementary Information.

References

1. Janek, J. & Zeier, W. G. Challenges in speeding up solid-state battery development. *Nat. Energy* **8**, 230–240 (2023).
2. Xiao, Y. et al. Understanding interface stability in solid-state batteries. *Nat. Rev. Mater.* **5**, 105–126 (2019).
3. Han, F. et al. High electronic conductivity as the origin of lithium dendrite formation within solid electrolytes. *Nat. Energy* **4**, 187–196 (2019).
4. Ye, L. & Li, X. A dynamic stability design strategy for lithium metal solid state batteries. *Nature* **593**, 218–222 (2020).
5. Chen, Y. et al. Li metal deposition and stripping in a solid-state battery via Coble creep. *Nature* **578**, 251–255 (2020).
6. Han, X. et al. Negating interfacial impedance in garnet-based solid-state Li metal batteries. *Nat. Mater.* **16**, 572–579 (2017).
7. Zhao, Q., Stalin, S., Zhao, C. Z. & Archer, L. A. Designing solid-state electrolytes for safe, energy-dense batteries. *Nat. Rev. Mater.* **5**, 229–252 (2020).
8. Yang, X. et al. Determining the limiting factor of the electrochemical stability window for PEO-based solid polymer electrolytes: main chain or terminal –OH group? *Energy Environ. Sci.* **13**, 1318–1325 (2020).
9. Banerjee, A., Wang, X., Fang, C., Wu, E. A. & Meng, Y. S. Interfaces and interphases in all-solid-state batteries with inorganic solid electrolytes. *Chem. Rev.* **120**, 6878–6933 (2020).
10. Lee, Y. G. et al. High-energy long-cycling all-solid-state lithium metal batteries enabled by silver–carbon composite anodes. *Nat. Energy* **5**, 299–308 (2020).
11. Zhou, L. et al. High areal capacity, long cycle life 4 V ceramic all-solid-state Li-ion batteries enabled by chloride solid electrolytes. *Nat. Energy* **7**, 83–93 (2022).
12. Mohandas, K. S., Sanil, N. & Rodriguez, P. Development of a high temperature conductance cell and electrical conductivity measurements of $MAlCl_4$ (M = Li, Na and K) melts. *Trans. Inst. Min. Metall. C.* **115**, 25–30 (2006).
13. Tanibata, N. et al. Metastable chloride solid electrolyte with high formability for rechargeable all-solid-state lithium metal batteries. *ACS Mater. Lett.* **2**, 880–886 (2020).

14. Park, J. et al. NaAlCl4: new halide solid electrolyte for 3 V stable cost-effective all-solid-state Na-ion batteries. *ACS Energy Lett.* **7**, 3293–3301 (2022).
15. Weppner, W. & Huggins, R. A. Ionic conductivity of alkali metal chloroaluminates. *Phys. Lett. A* **58**, 245–248 (1976).
16. Flores-González, N. et al. Mechanochemical synthesis and structure of lithium tetrahaloaluminates, $LiAlX_4$ (X = Cl, Br, I): a family of Li-Ion conducting ternary halides. *ACS Mater. Lett.* **3**, 652–657 (2016).
17. Einarsrud, M. A., Rytter, E. & Ystenes, M. Experimental and theoretical spectra of stoichiometric complex ions in oxochloroaluminate melts. *Vib. Spectrosc.* **1**, 61–68 (1990).
18. Berg, R. W. Ab initio MO calculations on the structure and Raman and infrared spectra of $[Al_4O_2Cl_{10}]^{2-}$ oxide in chloroaluminate melts. *Z. Naturforsch. A* **62**, 157–168 (2007).
19. Turnbull, D. & Cohen, M. H. Free-volume model of the amorphous phase: glass transition. *J. Chem. Phys.* **34**, 120–125 (1961).
20. Ayame, A. & Kitagawa, T. X-Ray photoelectron spectroscopic measurement and chemical characteristics of silica, alumina and silica-alumina. *Bunseki Kagaku* **40**, 673–678 (1991).
21. Maiti, S. et al. Understanding the role of alumina (Al_2O_3), pentalithium aluminate (Li_5AlO_4), and pentasodium aluminate (Na_5AlO_4) coatings on the Li and Mn-rich NCM cathode material 0. $33Li_2MnO_3{\cdot}0.67Li(Ni_{0.4}Co_{0.2}Mn_{0.4})O_2$ for enhanced electrochemical performance. *Adv. Funct. Mater.* **31**, 202008083 (2020).
22. Yu, Y., Wang, Z. & Shao, G. Formulation of Li-metal-halide (LMX) solid state electrolytes through extensive first principles modelling. *J. Mater. Chem. A* **9**, 25585–25594 (2021).
23. Xiao, Y. et al. Electrolyte melt infiltration for scalable manufacturing of inorganic all-solid-state lithium-ion batteries. *Nat. Mater.* **20**, 984–990 (2021).
24. Nam, Y. J., Oh, D. Y., Jung, S. H. & Jung, Y. S. Toward practical all-solid-state lithium-ion batteries with high energy density and safety: Comparative study for electrodes fabricated by dry- and slurry-mixing processes. *J. Power Sources* **375**, 93–101 (2018).
25. Kwak, H. et al. Emerging halide superionic conductors for all-solid-state batteries: design, synthesis, and practical applications. *ACS Energy Lett.* **7**, 1776–1805 (2022).
26. Zhong, Y. et al. A highly efficient all-solid-state lithium/electrolyte interface induced by an energetic reaction. *Angew. Chem.* **59**, 14003–14008 (2020).
27. Oh, J. A. S. et al. A robust solid-solid interface using sodium-tin alloy modified metallic sodium anode paving way for all-solid-state battery. *Adv. Energy Mater.* **11**, 2101228 (2021).
28. Kresse, G. & Furthmüller, J. Efficient iterative schemes for ab initio total-energy calculations using a plane-wave basis set. *Phys. Rev. B* **54**, 11169 (1996).
29. Perdew, J. P., Burke, K. & Ernzerhof, M. Generalized gradient approximation made simple. *Phys. Rev. Lett.* **77**, 3865 (1996).
30. Wang, H., Zhang, L., Han, J. & Weinan, E. DeePMD-kit: a deep learning package for many-body potential energy representation and molecular dynamics. *Comput. Phys. Commun.* **228**, 178–184 (2018).
31. Thompson, A. P. et al. LAMMPS-a flexible simulation tool for particle-based materials modeling at the atomic, meso, and continuum scales. *Comput. Phys. Commun.* **271**, 108171 (2022).
32. Wu, S., Xiao, R., Li, H. & Chen, L. New insights into the mechanism of cation migration induced by cation–anion dynamic coupling in superionic conductors. *J. Mater. Chem. A Mater.* **10**, 3093–3101 (2022).
33. Momma, K. & Izumi, F. VESTA 3 for three-dimensional visualization of crystal, volumetric and morphology data. *J. Appl. Crystallogr.* **44**, 1272–1276 (2011).
34. Toby, B. H. & Von Dreele, R. B. GSAS-II: the genesis of a modern open-source all purpose crystallography software package. *J. Appl. Crystallogr.* **46**, 544–549 (2013).
35. Farrow, C. L. et al. Billinge, PDFfit2 and PDFgui: computer programs for studying nanostructure in crystals. *J. Phys. Condens. Matter* **19**, 335219 (2007).

Acknowledgements

This work was supported by the National Natural Science Foundation of China (52122214) and the Youth Innovation Promotion Association of the Chinese Academy of Sciences (2020006). We thank H. Chen and W. Yin at the Spallation Neutron Source Science Center (SNSSC), Dongguan, China for their great support with the neutron total scattering experiments.

Author contributions

Y.S.H. and T.D. conceived the research. T.D. performed the experiments with Y.X.L. T.D. determined the composition with J.Z. S.W. carried out the simulation work with R.X. Y.Y. and Y.L. completed the XPS experiments and analysed the NPD data. C.C. conducted the DMA tests with Y.L. and W.W. T.D., Y.X.L. and Y.S.H. wrote the manuscript. All authors participated in analysing the experimental results and preparing the manuscript.

Competing interests

Y.S.H. is employed by HiNa Battery Technology Co. Ltd. The other authors declare no competing interests.

Additional information

Supplementary information The online version contains supplementary material available at https://doi.org/10.1038/s41560-023-01356-y.

Correspondence and requests for materials should be addressed to Yaxiang Lu, Junmei Zhao or Yong-Sheng Hu.

Peer review information *Nature Energy* thanks Naoto Tanibata, Thomas A. Yersak and the other, anonymous, reviewer(s) for their contribution to the peer review of this work.

Reprints and permissions information is available at www.nature.com/reprints.